

A model of decentralized vision in the sea urchin *Diadema africanum*

Tianshu Li^{a,b,c}, John Kirwan^{d,e}, Maria Ina Arnone^d, Dan-Eric Nilsson^e,
Giancarlo La Camera^{a,b,c,1}

^a Department of Neurobiology & Behavior, Stony Brook University, Stony Brook, NY, USA

^b Program in Neuroscience, Stony Brook University, Stony Brook, NY, USA

^c Center for Neural Circuit Dynamics, Stony Brook University, Stony Brook, NY, USA

^d Stazione Zoologica Anton Dohrn, Naples, Italy

^e Lund Vision Group, Department of Biology, Lund University, Lund, Sweden

Abstract

Sea urchins can detect light and move in relation to luminous stimuli despite lacking eyes. They presumably detect light through photoreceptor cells distributed on their body surface. However, there is currently no mechanistic explanation of how these animals can process light to detect visual stimuli and produce oriented movement. Here, we present a model of decentralized vision in echinoderms that includes all known processing stages, from photoreceptor cells to radial nerve neurons to neurons contained in the oral nerve ring encircling the mouth of the animals. In the model, light stimuli captured by photoreceptor cells produce neural activity in the radial nerve neurons. In turn, neural activity in the radial nerves is integrated in the oral nerve ring to produce a profile of neural activity reaching spatially across several ambulacra. This neural activity is read out to produce a model of movement. The model captures the pattern of behavior observed in sea urchin *Diadema africanum* probed with a variety of physical stimuli. The specific pattern of neural connections used in the model makes testable predictions on the properties of single neurons and aggregate neural behavior in *Diadema africanum* and other echinoderms, offering a potential understanding of the mechanism of visual orientation in these animals.

¹Address correspondence to Giancarlo La Camera, Department of Neurobiology and Behavior, Stony Brook University, Stony Brook, NY. Email: giancarlo.lacamera@stonybrook.edu.

Contents

1	Introduction	3
2	Methods	4
2.1	Experimental setup	4
2.2	Stimuli	4
2.3	Vision model	7
2.3.1	General anatomical features	7
2.3.2	Photoreceptor cells (PRCs)	9
2.3.3	Radial nerve neurons	12
2.3.4	Oral nerve ring	13
2.4	Behavioral model	13
2.4.1	Population vector and direction of movement	13
2.4.2	Inference of visual detection based on the population vector	14
2.4.3	Model of movement	15
2.4.4	Simulations of behavioral trajectories	15
3	Results	17
3.1	Model prediction of object taxis in <i>Diadema africanum</i>	17
3.2	Prediction of behavioral trajectories	19
3.3	Effect of location and acceptance angle of PRCs on spatial vision	19
4	Discussion	22
4.1	A model of decentralized vision in sea urchins	22
4.2	Lessons from lesion studies	22
4.3	Input from mammalian physiology	23
4.4	Questions for future experiments	24
5	Acknowledgments	24
A	Supplementary information	25
A.1	Analytical formula for the preferred directions of eONR cells	25
A.2	Neural activity and population vector as a function of animal orientation	27
A.3	Simulation of behavioral trajectories	27
A.4	The effect of variability on PRCs' acceptance angles	27
	References	29

1 Introduction

Sea urchins are a large clade of echinoderms and are predominantly night-active herbivores inhabiting shallow seas. Despite lacking eyes, these marine animals can visually resolve objects and move towards them, as well as point their spines towards looming visual stimuli (Holmes, 1912; Millott and Takahashi, 1963; Yoshida, 1966; Blevins and Johnsen, 2004; Yerramilli and Johnsen, 2010; Al-Wahaibi and Claereboudt, 2017; Kirwan et al., 2018). The long-spined sea urchin *Diadema africanum* (Rodríguez et al., 2013), a night-active, herbivorous diadematoid of the eastern Atlantic, moves towards dark objects with a spatial resolution of 29–69° (Kirwan et al., 2018), i.e. 0.01–0.03 cycles per degree. Such behavior is normally associated with a centralized brain processing visual information from discrete eyes, yet sea urchins lack both. Therefore, sea urchins possess a unique visual system which has not been studied in terms of its information processing. Here, we set out to provide a mechanistic model of directional, low resolution vision in sea urchins building on our knowledge of their general neural anatomy and the behavior observed in *D. africanum*.

In adult sea urchins, resolving vision may be mediated by photoreceptor cells (PRCs) situated in the tube feet of the animal. The tube feet emerge from five vertical grooves in the animal endoskeleton called ‘ambulacra’, located with pentaradial symmetry on the body surface. The tube feet are involved in such tasks as locomotion, positioning, cleaning and feeding (Hyman, 1955), but each tube foot also has PRCs (Agca et al., 2011; Lesser et al., 2011; Ullrich-Lüter et al., 2011). The anatomical and molecular description of PRCs in sea urchins come mostly from studies in the species *Strongylocentrotus purpuratus*, where it has been found that PRCs along the tube feet are shielded such that they only detect light from a restricted angle, approximately orthogonal to the body surface (Woodley, 1982; Blevins and Johnsen, 2004; Yerramilli and Johnsen, 2010; Ullrich-Lüter et al., 2011). Due to this property, the PRCs on the tube feet can together provide coarse spatial information as if the entire animal was a compound eye (Blevins and Johnsen, 2004; Ullrich-Lüter et al., 2011). However, sea urchins have no centralized brain which could process light information coming from the PRCs; rather, their internal nervous system comprises five radial nerves (RNs) and one oral nerve ring (ONR). The ONR is a commissure surrounding the mouth and interconnecting the RNs, and therefore is ideally poised to be responsible for both sensory integration and motor coordination, as previously suggested (see e.g. (Yoshida, 1966) and our Discussion).

In the model presented in this work, light information from PRCs is processed in the RNs and then relayed to ONR neurons, whose activity is read out to produce visually guided behavior. We apply our model to explain the behavior of *D. africanum* in the presence of isoluminant visual stimuli with a central dark ‘target’ flanked by lighter regions (Kirwan et al., 2018). *D. africanum* also displays a spine-pointing response to looming circular fields subtending 13–25 degrees (Kirwan et al., 2018); here, however, we focus on modeling the movement towards stimuli that are isoluminant to the background as this allows to discriminate spatial vision from phototaxis. In the experiments, the animals were initially placed at the center of a circular arena, with stimuli placed on its outer wall; the animals would then move towards the wall of the arena, and their behavior was analyzed in search for patterns of directional motion. The model presented here makes testable predictions on the behavior in this setup for a large class of visual stimuli, in particular on the three stimuli tested in the experiments of Kirwan et al. (2018). For these stimuli, the distribution of final positions predicted by the model matches, to a remarkable degree, the distribution of final positions reached by the animals.

To our knowledge, this is the first model of decentralized vision and visually-guided behavior in sea urchins. The model combines all known neural processing stages, from PRCs to RN neurons to ONR neurons, including a probabilistic readout mechanism of the activity of ONR neurons that is responsible for visually-guided movement. The specific pattern of neural connections used in the model also makes

testable predictions on the properties of single neurons in each processing stage, such as their cell type (inhibitory vs. excitatory), their connectivity structure, and their response properties. All of these properties can in principle be measured in experiment and may lead to an understanding of the mechanism of visually guided orientation in echinoderms.

2 Methods

2.1 Experimental setup

Here we briefly describe the setup for the taxis experiments reported in (Kirwan et al., 2018). Individual sea urchins of the species *D. africanum* were placed in a lit arena, surrounded by printed patterns containing a printed visual stimulus (Fig. 1). The arena comprised a cylinder of transparent acrylic and was surrounded by a white cylinder to exclude external cues. An array of four equidistant clusters of LEDs resulting in broad-spectrum visible illumination were placed above the arena. A remote-controlled camera was attached in an opening in an illumination diffuser at the top of the arena and was used to record time-lapse videos at a rate of 5 frames per second. The arena was filled with filtered natural seawater, at the same temperature at which the animals were housed (20°C). In each trial, the animal was placed by hand in the center of the arena and allowed to move to the periphery. Each trial continued for a maximum of 6 min or until the animal approached the arena wall. A trial was deemed complete if the animal moved at least three-quarters of the radial distance between the center and arena walls. Trials were conducted in sets of four and the stimulus was moved 90° clockwise for each subsequent trial, to remove the influence of any non-visual directional cues. Sets with individuals for which there were fewer than four completed trials (e.g. due to a loss of motivation) were excluded from analysis. The base of the arena was cleaned between trial sets with a brush to obscure chemical cues and the water was partially or completely changed, depending on its clarity. Experiments were performed during the daylight period of their entrainment. The frame rate for the recordings was 1 frame/s. Full details can be found in (Kirwan et al., 2018).

2.2 Stimuli

The printed patterns surrounding the arena consisted of greyscale printed images, which were uniform in the vertical plane but in the horizontal plane included stimuli that consisted of dark regions set against a lighter background (Fig. 1B). The main patterns used a bar stimulus and a difference of Gaussians (DoG). In the bar stimulus, a region of homogeneously black stimulus was presented against a white background. In the DoG stimulus, the center of the stimulus was maximally dark, but of increasing reflectance towards the periphery of the stimulus (on the horizontal axis) and reaching the maximum achievable reflectance before darkening into the grey background. All stimuli were isoluminant with respect to the remainder of the patterns due to the lighter regions flanking the stimulus, i.e., it is not possible to detect the stimulus by simply comparing the radiance profile of different parts of the arena from the centre without having a spatial resolution equivalent to the arc subtended by the stimulus itself.

In the following we refer to the stimulus as the entire pattern surrounding the arena wall. The intensity of the stimuli along the longitudinal (horizontal) dimension were indexed by an angle $\phi \in [0, 360]^{\circ}$, formed by an arbitrary reference line and the line connecting the center of the arena to the point of interest on the wall (we use degree ($^{\circ}$) as the angle units in this paper). The normalized light intensity of a stimulus at ϕ , $X_0(\phi)$ (henceforth simply ‘intensity’), indicates the reflectance of the stimulus at an angle ϕ from

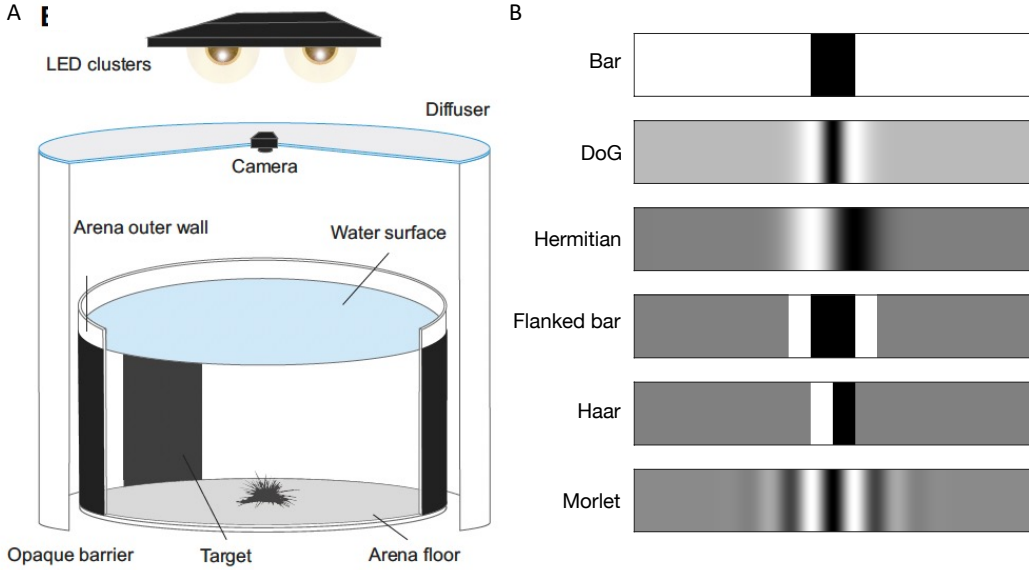


Figure 1: Experimental setting and stimuli. **A.** Behavioral experiment setting. The stimuli were attached on the outer wall of the arena. At the beginning of each trial, the animal was positioned at the center of the arena with a random orientation. **B.** Examples of the six stimuli used in this work with $\phi_{stim} = 40^\circ$ (mathematical definitions in Table 1). The ink value of black and white are 1 and 0, respectively. Panel A adapted from (Kirwan et al., 2018).

the center and varied linearly from 0.176 to 1 (Kirwan et al., 2018):

$$X_0(\phi) = 0.824(1 - X_{ink}(\phi)) + 0.176, \quad (1)$$

where X_{ink} was the ink value used in the actual experiments to print the images on the arena outer wall (Fig. 1B: the ink value of black is 1, for white is 0). Since photoreceptor cells respond to light, we replaced X_{ink} with $1 - X_{ink}$ to convert the ink value to the intensity of light reflected by the stimulus in Eq. 1. Moreover, in Eq. 1 we also took into account the relative reflectance of the paper (only a proportion of the light was reflected by the paper) (Kirwan et al., 2018). To obtain X_{ink} values between 0 and 1, we started from the functions $X_{ink,raw}$ reported in Table 1, and then rescaled $X_{ink,raw}$ by a simple linear normalization:

$$X_{ink} = \frac{X_{ink,raw} - \min_\phi X_{ink,raw}(\phi)}{\max_\phi X_{ink,raw}(\phi) - \min_\phi X_{ink,raw}(\phi)}. \quad (2)$$

In addition to the stimuli above, we also used a homogeneous stimulus of constant intensity $X_0(\phi) = 0.77$ as control (same as the intensity of the DoG stimulus away from its center).

Note that each stimulus had an intuitively clear ‘center’ (Fig. 1B), which was always aligned to the reference line (i.e., the center of the stimulus was always at $\phi = 0^\circ$ on the wall of the arena). The center of each stimulus was characterized by an arc width ϕ_{stim} which encloses the high amplitude region of the stimulus, surrounding the center. For example, in the case of the bar stimulus (see Fig. 1B), ϕ_{stim} corresponds to the arc width of the black region, while for the DoG it corresponded to the arc width of the distance between the two white maxima.

VISUAL STIMULI

Bar	$X_{ink,raw}(\phi) = \begin{cases} 1 & \text{if } \phi \in [0, \frac{\phi_{stim}}{2}] \cup [360^\circ - \frac{\phi_{stim}}{2}, 360^\circ) \\ 0 & \text{otherwise} \end{cases}$
Difference of Gaussians (DoG)	$\sigma_1 = \frac{\phi_{stim}}{2\sqrt{2 \ln 2}}$ $\sigma_2 = 2\sigma_1$ $X_{ink,raw}(\phi) = e^{-\frac{\phi^2}{2\sigma_1^2}} - \frac{\sigma_1}{\sigma_2} e^{-\frac{\phi^2}{2\sigma_2^2}}$
1st Hermitian wavelet	$D = \frac{2\phi_{stim}}{2\sqrt{3}\sqrt{2 \ln 2}}$ $g(\phi) = e^{-\frac{\phi^2}{2D^2}}$ $X_{ink,raw}(\phi) = -g'(\phi)$
Flanked bar (FB)	$X_{ink,raw}(\phi) = \begin{cases} 1 & \text{if } \phi \in [0, \frac{\phi_{stim}}{2}] \cup [360^\circ - \frac{\phi_{stim}}{2}, 360^\circ) \\ 0 & \text{if } \phi \in [\frac{\phi_{stim}}{2}, \phi_{stim}] \cup [360^\circ - \phi_{stim}, 360^\circ - \frac{\phi_{stim}}{2}) \\ 0.5 & \text{otherwise} \end{cases}$
Haar wavelet	$X_{ink,raw}(\phi) = \begin{cases} 1 & \text{if } \phi \in [0, \frac{\phi_{stim}}{2}] \\ 0 & \text{if } \phi \in [360^\circ - \frac{\phi_{stim}}{2}, 360^\circ) \\ 0.5 & \text{otherwise} \end{cases}$
Morlet wavelet	$D = \frac{2\phi_{stim}}{2\sqrt{2 \ln 2}}$ $X_{ink,raw}(\phi) = e^{-\frac{\phi^2}{2D^2}} \cos(\frac{2\pi\phi}{\phi_{stim}})$

Table 1: Mathematical definitions of the stimuli of Fig. 1B. The rightmost column contains the formulae for $X_{ink,raw}(\phi)$ for each stimulus.

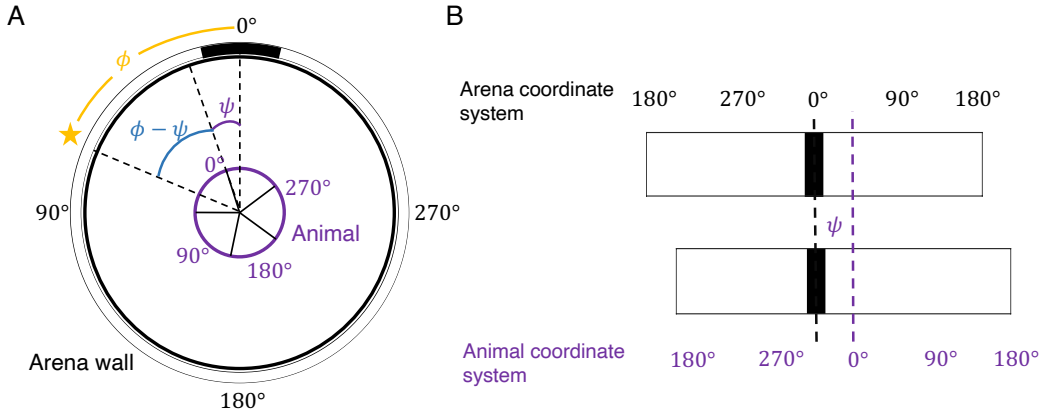


Figure 2: Light intensity in the reference frame of the sea urchin. **A.** Diagram of a $\phi_{stim} = 40^\circ$ bar stimulus attached to the arena outer wall (black circle). Black numbers outside of the arena indicate the arena’s coordinate system. A sea urchin (purple circle) is placed at the center of the arena. Black solid lines originating from the center of the arena represent the ambulacra. One ambulacrum, here positioned at angle $\phi = 30^\circ$, is randomly chosen to be the ‘first ambulacrum’ and is the reference direction in the animal’s own coordinate system (purple numbers). The value of the ink at the location indicated by the yellow star is $X_{ink}(\phi) = 0$, and the light intensity at this location is $X(\phi - \psi) = X_0(\phi) = 0.884(1 - X_{ink}(\phi)) + 0.036 = 0.92$. **B.** The top band is the stimulus paper in A cut at 180° in the arena’s coordinate system (black numbers at the top). The bottom band is the stimulus paper cut at 180° in the animal’s coordinate system (purple numbers at the bottom).

We next define the intensity of the stimulus in the animals’ own coordinate system, defined by the longitudinal angle ψ between the ‘first ambulacrum’ (arbitrarily chosen) and the origin of the arena’s coordinate system. The angle ψ defines the orientation of the animal in the arena, which is assumed constant during motion (i.e., the animal does not rotate as it moves; see also Sec. 2.4.4). Therefore, each animal has its own (constant) value of ψ . This is illustrated in Fig. 2A, showing a cartoon of the arena (black circle) with a sea urchin (purple circle) placed at the center of the arena. Black numbers outside the arena are coordinates in the arena’s coordinate system, while purple numbers are the coordinates in the sea urchin’s system. In the animal’s coordinate system, the intensity of light at angle ϕ is given by

$$X(\phi - \psi) = X_0(\phi). \quad (3)$$

In our model, this quantity was the input to the photoreceptor cells distributed on the tube feet of the animal (see Eq. 5).

2.3 Vision model

2.3.1 General anatomical features

We constructed a model of vision in *Diadema africanum* by integrating three main components: photoreceptor cells (PRCs), radial nerves (RNs) and oral nerve ring (ONR). PRCs and RNs were located along each of the five ambulacra; the PRCs were located outside the test, along tube feet ([Ullrich-Lüter et al., 2011](#)), while the neurons were located inside the test along the latitudinal direction (Fig. 3A). For convenience, we grouped the PRCs in separate groups according to their target neurons in the RNs, and we did the same for the RN neurons (Fig. 3B). The numbers of groups of PRCs and RN neurons in

ambulacrum k were N_{PRC}^k and N_{RN}^k , respectively (see Table 2). Similarly, we divided the ONR neurons in two subgroups, excitatory and inhibitory, and each subgroup was further divided into N_{ONR} groups based on the patterns of connectivity (details below). The number of neurons in each group need not be specified, since it can always be changed by rescaling the connection weights, as will be clearer in a later section (see e.g. Eq. 6). Since sea urchins have five-fold symmetry, the center position of ambulacrum k was set to be $\phi^k = 72(k - 1)^\circ$. Since the stimuli were vertically homogeneous, we simplified the 3D structure of the test to a horizontal slice (Fig. 3A).

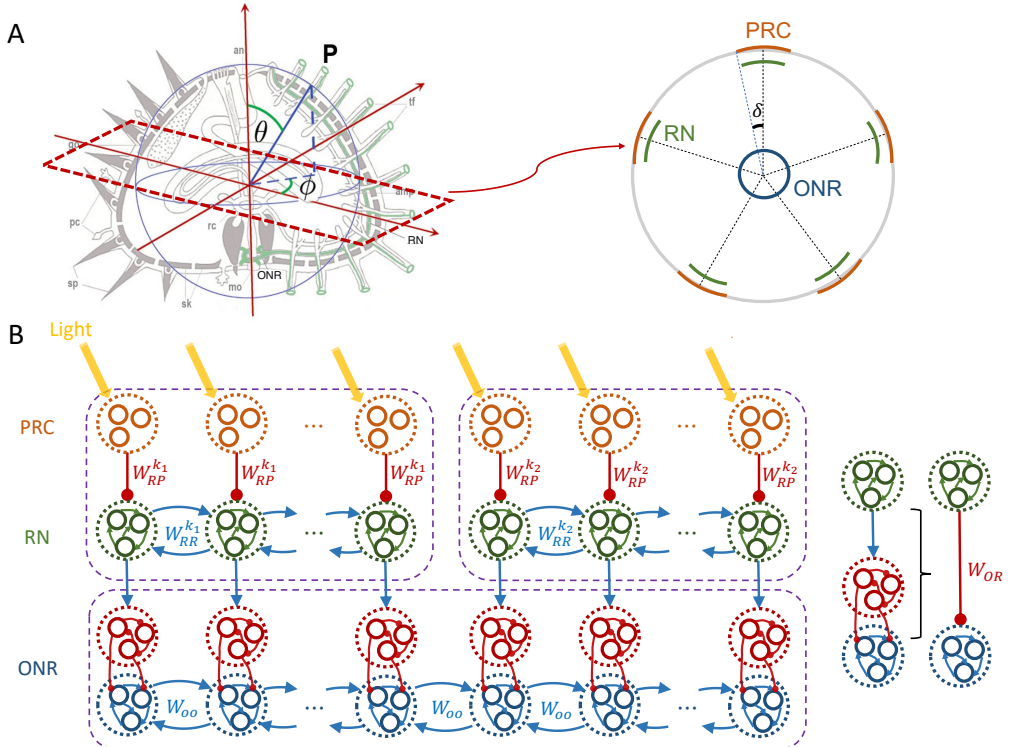


Figure 3: Schematic illustration of the model nervous system. **A** Schematic geometry of the animal. Left: 3D geometry. Right: transverse view of the animal cut above the ONR. The orange arcs indicate the distributions of PRCs on each ambulacrum (δ : half width of the distribution). The green arcs indicate RN cells. The blue circle indicates eONR cells. **B** Cartoon of the network structure used in the model (only 2 ambulacra shown at the top, represented by purple rectangles). Red segments terminating in a circle indicate inhibitory connections, blue arrows indicate excitatory connections. From top to bottom, orange circles indicate groups of PRCs, green circles indicate groups of RN neurons, red circles indicate groups of iONR neurons, and blue circles indicate groups of eONR neurons. The rightmost sketch illustrates how the action of RN cells onto eONR cells results into an effective inhibition of the latter.

As information flows from PRCs to RN neurons to ONR neurons, the model can be abstracted as comprising three major layers. The model has feedforward connections between the layers (PRCs to RN neurons and RN neurons to ONR neurons) as well as recurrent connections among neurons in the same RN, and within neurons of the ONR (Fig. 3B). Once activated by light, PRCs inhibit connected groups of RN neurons on the same ambulacrum. RN neurons were assumed to be excitatory, with different RN neuron groups exciting one another. The same groups of RN neurons send excitatory projections to input

stage inhibitory cells in the ONR (iONR cells). The latter inhibit the activity of downstream groups of excitatory ONR neurons (eONR cells), that could be interpreted as the output sublayer of ONR. In turn, these groups of eONR neurons excite one another via recurrent connections (Fig. 3B). This allows to integrate information across the five ambulacra, thus mediating a form of decentralized vision.

This anatomical organization results in light-induced excitation of eONR neurons by double inhibition (PRCs \rightarrow RNs and RNs \rightarrow eONR via excitation of iONR). Although this is not the only possible mechanism compatible with our results, we favored double inhibition over double excitation because the former makes our model compatible with results obtained by Yoshida in sea urchin *Temnopleurus torematicus* (Yoshida, 1966) (see Discussion, Sec. 4.2, for details).

Note that although sea urchins can presumably sense light gradients along the latitudinal direction, we did not consider this possibility in our model, since our stimuli were vertically homogeneous and locomotion occurred always on a horizontal plane. We also grouped cells with similar properties in each layer (PRC, RN or ONR) and averaged their behavior (input and output), so that we can consider a homogeneous group of neurons as the elementary processing unit in our model. The details of the input-output function of each unit are given in the next subsections. This type of coarse-grained approach is typically successful in systems with redundant numbers of elements and it allows to focus on the essential features of the anatomy. The model can be refined as more detailed information about the anatomy of sea urchins is obtained (see also the Discussion).

MODEL PARAMETERS

Symbol	Description	Value
N_{PRC}^k	Number of groups of PRCs on the k th ambulacrum	100
N_{RN}^k	Number of groups of RNs on the k th ambulacrum	100
N_{ONR}	Number of groups of eONR neurons (same for iONR neurons)	500
$\Delta\rho$	Acceptance angle of PRCs (width at half max of angular sensitivity function)	30°
δ	Half-width of the distribution of PRCs locations on each ambulacrum	15°
$r_{i,max}^{k,PRC}$	Maximal activity of the i th PRC on ambulacrum k	1
$r_{i,max}^{k,RN}$	Maximal activity of the i th RN on ambulacrum k	1
$r_{i,max}^{ONR}$	Maximal activity of the i th ONR	1
a_{RR}	Strength of the lateral connection weights in the RNs	0.25
a_{OO}	Strength of the lateral connection weights in the ONR	0.25
β_{RN}	Steepness of RN's sigmoidal response function	3
θ_{RN}	Location parameter of RN's sigmoidal response function	-1.8
β_{ONR}	Steepness of ONR's sigmoidal response function	4.5
θ_{ONR}	Location parameter ONR's sigmoidal response function	-2
θ_p	Threshold for population vector length	5
δr	Length of each step when generating trajectory	0.1

Table 2: Description and numerical values of the model parameters.

2.3.2 Photoreceptor cells (PRCs)

PRCs are located inside the tube feet protruding along each ambulacrum (Burke et al., 2006; Ullrich-Lüter et al., 2011). The available anatomical description of PRCs, coming mostly from studies in the species *Strongylocentrotus purpuratus* (Agca et al., 2011; Lesser et al., 2011; Ullrich-Lüter et al., 2011), is

still incomplete. In the absence of more detailed information about the spatial distribution of PRCs, we assume a uniform distribution of PRCs in each ambulacrum. Since changes along the latitudinal direction are not relevant in our model, we focus again on the longitudinal direction. Along the k th ambulacrum, we assume a uniform distribution between of PRCs between $\phi^k - \delta$ and $\phi^k + \delta$, where ϕ^k is the position of the center of the ambulacrum (we used $\delta = 15^\circ$ in the main simulations; see Table 2). Each PRC had an acceptance angle of $\Delta\rho = 30^\circ$. The acceptance angle is the width at half maximum of the normalized angular sensitivity curve of the PRCs (see below).

The chosen value of the PRCs acceptance angle is the consequence of the position of the PRCs on the tube feet and other factors, such as depressions in the test that can hold space for r-opsin expressing PRCs while also screening light reaching the PRCs (Ullrich-Lüter et al., 2011), or the shading activity of opaque spines (Woodley, 1982; Blevins and Johnsen, 2004; Yerramilli and Johnsen, 2010). Regardless of the specific mechanism, our behavioral experiments (Kirwan et al., 2018) suggest acceptance angles in the range 38° - 89° . As this estimate takes also into account the distribution width of PRC locations on each ambulacrum, here quantified by δ , we chose $\Delta\rho = 30^\circ$ so as to obtain an ‘effective’ acceptance angle of $\Delta\rho_{eff} = \Delta\rho + 2\delta = 60^\circ$. Also note that, while it is unrealistic to use a single value for all acceptance angles, assigning a specific value to each different PRC is impractical. The most effective way to deal with this situation is to draw the values of $\Delta\rho$ and δ from suitable random distributions. We checked that doing so does not significantly alter our results (Supplementary Information, Sec. A.4).

Each PRC had a direction of maximal sensitivity to light, with response dwindling for surrounding directions (angular sensitivity curve). Typically the angular sensitivity curve is modeled by a Gaussian function normalized to have a unitary peak, possibly cut-off at its tails (Land and Nilsson, 2012). We approximated such a function with a cosine function (Georgopoulos et al., 1982; Salinas and Abbott, 1994) that optimally matches the Gaussian function away from its tails, while naturally vanishing in the corresponding tail regions:

$$f_i^k(\phi) = \left[\frac{\cos(\phi - \phi_{i,dms}^{k,PRC}) - a}{1 - a} \right]_+. \quad (4)$$

In this function, f_i^k is the response of the i th PRC on ambulacrum k , $a = 2 \cos(\Delta\rho/2) - 1$, where $\Delta\rho$ is the acceptance angle of the PRC, and the symbol $[\cdot]_+$ means rectification ($[x]_+ \geq 0$ for $x \geq 0$, $[x]_+ = 0$ otherwise). $\phi_{i,dms}^{k,PRC}$ is the direction of maximum sensitivity of the i th PRC on ambulacrum k , and is also the actual location of the cell in the coordinate system of the sea urchin. Eq. 4 is plotted in Fig. 4A for PRCs in all five ambulacra (each ambulacrum in a different color).

The function $f_i^k(\phi)$ characterizes the response of PRCs to light coming from a punctiform source located at ϕ . The response of the same PRC to a full stimulus comprising light coming from all directions ϕ with intensity $X(\phi)$, was obtained by integrating the input X along the angular dimension, weighted by the angular sensitivity curve f_i^k :

$$r_i^{k,PRC} = \frac{r_{i,max}^{k,PRC}}{Z_i^{k,PRC}} \int_0^{360^\circ} d\phi X(\phi) f_i^k(\phi), \quad (5)$$

where $Z_i^{k,PRC} = \int_0^{360^\circ} d\phi f_i^k(\phi)$ is a normalization factor to keep the output activity of PRCs in a physiological range (note that $X(\phi) \leq 1$ for all stimuli). The output is proportional to $r_{i,max}^{k,PRC}$, a constant parameter with physical units of PRC activity. Note that for our choice of stimuli and parameters, $r_i^{k,PRC} \leq r_{i,max}^{k,PRC}$.

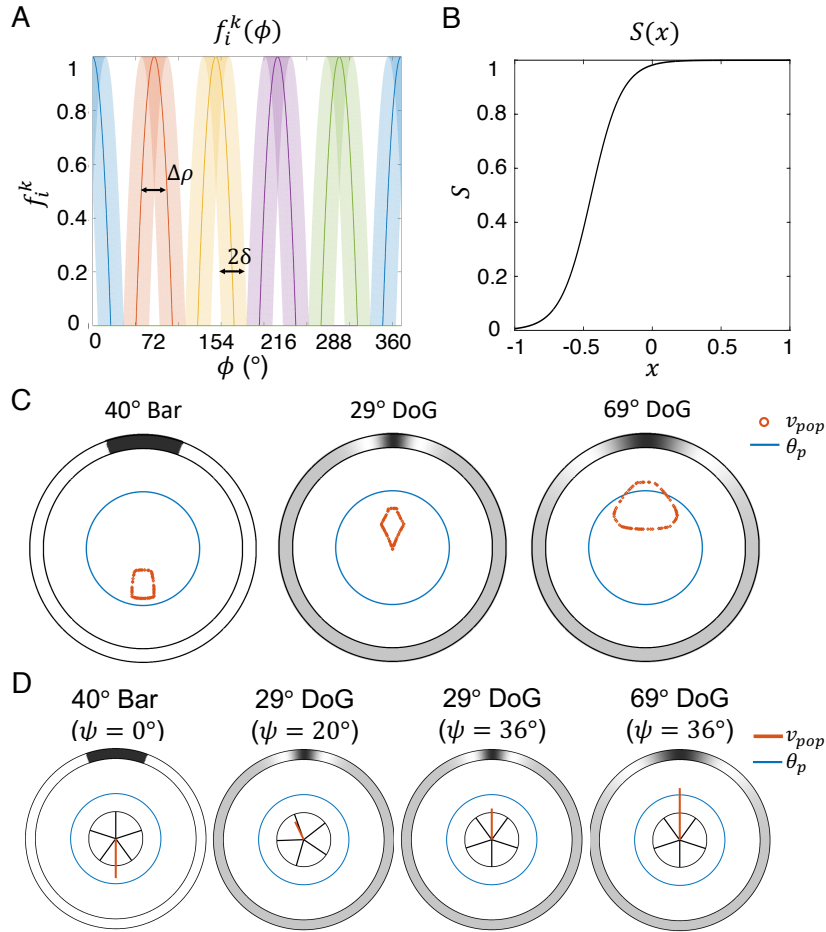


Figure 4: Angular sensitivity curves and population vectors.

A. Angular sensitivity curves of PRC $f_i^k(\phi)$ (Eq. 4 with $\Delta\rho = 30^\circ$ and $\delta = 15^\circ$). Each color represents an ambulacrum. The light shades represent the angular sensitivity curves of all PRCs (uniformly distributed with half-width δ in each ambulacrum). The darker lines are examples of single angular sensitivity curves (one example for each ambulacrum). **B.** Plot of sigmoidal function S (Eq. 9 with $\beta = 4.5$ and $\theta = -2$) used to model the output of RN and ONR neurons. Note that activation of PRCs results in a reduced overall input x , reducing the output of RN cells (see the text). **C.** Population vectors (readout of eONR cells, Eq. 13) for three stimuli: 40° bar, 29° DoG and 69° DoG (from left to right). Note that each data point (red circle) corresponds to the tip of one population vector. Different population vectors were obtained by varying the orientation of the sea urchin with respect to the center of the stimulus (here, located at the top of the arena). All orientations (from 0° to 359°) are represented. The large blue circle is the threshold θ_p . If for a given orientation the population vector's length exceeds θ_p , coherent motion is predicted along the direction of the population vector. **D.** Examples of single population vectors among those in panel C for specific orientations (ψ) of the animal with respect to the center of the stimulus (see Fig. 2A).

2.3.3 Radial nerve neurons

Radial nerve neurons are also distributed along ambulacra (Cobb, 1970; Burke et al., 2006; Formery et al., 2021). In our model, we assumed that they receive inhibitory input from the PRCs (see Fig. 4 and Discussion). PRCs on ambulacrum k project to their target group of RN cells on the same ambulacrum via a (negative) connection weight W_{RP}^k . RN cells are also connected to other RN cells on the same ambulacrum k via a (positive) connection weight W_{RR}^k (see Fig. 3B). As illustrated in the figure, we assume that these ‘lateral’ connections among RN neurons are mostly local, i.e., they exist among spatially close groups of RN neurons, although this hypothesis is more a matter of convenience than a crucial ingredient of the model. We also note that these connections may or may not be established via chemical synapses – an issue that has not been settled, not even at the neuromuscular junction (Kawaguti, 1964; Florey and Cahill, 1980), but one that is not essential at our level of description.

Also for convenience, we scaled the connection weight as the inverse of the square root of the number of projecting groups of cells:

$$W_{RP}^k(i, j) = -1/\sqrt{N_{PRC}^k}, \quad (6)$$

$$W_{RR}^k(i, j) = a_{RR}/\sqrt{N_{RN}^k}, \quad (7)$$

where i, j are the indices of the cells connected by this weight (i is the index of the cell on the receiving end of the connection), and the parameter a_{RR} quantifies the strength of ‘lateral’ excitation in the RN layer of each ambulacrum. The scaling with the inverse square root of the total number of neurons echoes wisdom from mammalian physiology (Barral and Reyes, 2016). In this paper, however, this specific scaling is simply a means to parameterize the value of the connection strengths as a function of N_{PRC}^k and N_{RN}^k .

The activity of RN neurons in response to input coming from both PRCs and other RN neurons, measured in terms of firing rate, i.e., the number of action potentials emitted by these neurons in one second, was modeled as a sigmoidal function of the input (Fig. 4B):

$$r_i^{k,RN} = r_{i,max}^{k,RN} \mathcal{S} \left(\frac{W_{RP,(i)}^k \mathbf{r}^{k,PRC} + W_{RR,(i)}^k \mathbf{r}^{k,RN}}{|W_{RP,(i)}^k \mathbf{r}_{max}^{k,PRC}|} \right), \quad (8)$$

where $\mathcal{S}(x)$ is the sigmoidal function (see Fig. 4B)

$$\mathcal{S}(x) = \frac{1}{1 + e^{-2\beta(x-\theta)}}. \quad (9)$$

In Eq. 8, $r_i^{k,RN}$ is the output firing rate of the i th RN cell on ambulacrum k , $r_{i,max}^{k,RN}$ is the maximal firing rate (here, the same for all i), $\mathbf{r}^{k,PRC}$ and $\mathbf{r}^{k,RN}$ are vectors of activities from PRCs and RN cells, respectively, targeting RN cell i on ambulacrum k (these are visualized in Fig. 3B by the encircled groups of PRCs and RN neurons targeting the same group of RN neurons). The parameters β and θ define the shape of the sigmoidal function: its ‘center’ is located at θ and its steepness is given by β (for infinite steepness one obtains a step function). Finally, we have used the notation $W_{(i)}$ for the i th row of matrix W , and $W_{(i)}\mathbf{r}$ for the inner product of vectors $W_{(i)}$ and vector \mathbf{r} : $W_{(i)}\mathbf{r} = \sum_j W_{ij}r_j$.

Note that due to our choice of parameters and the fact that $W_{RP}^k < 0$, the argument of the output function $\mathcal{S}(x)$ is a monotonically decreasing function of the activity of the PRCs: the larger the PRC activity, the smaller the firing rate of RN neurons. In the absence of any input, the RN neurons maintain a spontaneous firing rate $\mathcal{S}(0) \times r_{i,max}^{k,RN} \approx r_{i,max}^{k,RN}$ (see Fig. 4B with $x = 0$). This amount of lateral input

to connected RN neurons brings the total output activity of RN neurons to its maximal value $r_{i,max}^{k,RN}$, which is therefore the level of activity of RN neurons in the absence of light (see Discussion, Sec. 4.2, for a justification of these assumptions).

2.3.4 Oral nerve ring

As outlined in Sec. 2.3.1, we assumed that the ONR contains inhibitory (iONR) and excitatory (eONR) neurons, with iONR neurons being the input stage of ONR. The RN cells project to iONR neurons via connection weights W_{iOR} , where the connection exists only between specific groups of iONR neurons and RN neurons in their vicinity, i.e., located on the ambulacrum closest to their target group. Groups of iONR neurons, in turn, inhibit groups of eONR neurons in their vicinity via connection weights $W_{eO_iO} < 0$. The overall effect of this connection pathway is inhibition of eONR neurons by RN input, and can be described as being mediated by effective (negative) connection weights W_{OR} (Fig. 3B). In turn, neighboring groups of eONR neurons are connected through (excitatory) weights W_{OO} . These lateral connections allow the ONR to integrate information coming from RNs on different ambulacula.

Similar to RN neurons, we rescaled the connection weights by the inverse square root of the total number of (groups of) neurons (note that $N_{ONR} = N_{RN} \doteq \sum_{k=1}^5 N_{NR}^k$):

$$W_{OR}(i,j) = -1/\sqrt{N_{ONR}}, \quad (10)$$

$$W_{OO}(i,j) = a_{OO}/\sqrt{N_{ONR}}. \quad (11)$$

Similarly to RN neurons, the output of eONR neurons is a sigmoidal function of their inputs,

$$r_i^{ONR} = r_{i,max}^{ONR} \mathcal{S} \left(\frac{W_{OR,(i)} \mathbf{r}^{RN} + W_{OO,(i)} \mathbf{r}^{ONR}}{|W_{OR,(i)} \mathbf{r}_{max}^{RN}|} \right), \quad (12)$$

where $\mathcal{S}(x)$ is Eq. 9. In Eq. 12, the meaning of the symbols is analogous to the meaning of the corresponding symbols for RN neurons in Eq. 8. In particular, \mathbf{r}^{RN} and \mathbf{r}^{ONR} are vectors of activities from RN (on all ambulacula) and ONR cells, respectively, targeting (directly or indirectly) eONR cell i , according to the connectivity pattern shown in Fig. 3B. The activity of ONR neurons increases due to lateral ONR input and decreases due to RN input.

2.4 Behavioral model

2.4.1 Population vector and direction of movement

Sea urchins can move towards or away from specific visual stimuli that they are able to detect (Yoshida, 1966; Blevins and Johnsen, 2004; Yerramilli and Johnsen, 2010; Kirwan et al., 2018; Al-Wahaibi and Claereboudt, 2017). In our model, the direction of movement was determined by pulling together the activity of eONR neurons to produce a specific vectorial readout named ‘population vector’. Only when the length of the readout exceeded a threshold θ_p would the animal produce coherent movement. Here, we describe how the population vector is built from the neural activity, while in Sec. 2.4.2 we present a possible readout of the population vector to infer the visual detection of a stimulus.

The population vector was built by first associating a vector to each eONR cell, \mathbf{z}_i^{ONR} , having direction given by the ‘preferred direction’ of the cell, $\phi_{i,pref}^{ONR}$. The preferred direction of an eONR cell was defined as the direction of a narrow stimulus causing the maximal increase in activity in the eONR cell. As the

narrow stimulus, we chose a 2° bar. Note that the preferred directions are properties of the cells and do not depend on the extended stimuli $X(\phi)$ (Table 1) used to probe movement; they can be computed analytically and agree with the preferred directions obtained in simulations with the 2° bar (we report the analytical details in the Supplementary Information, Sec. A.1). The preferred direction of an eONR cell was highly correlated with its angular position in the coordinate system of the animal, although, due to the lack of PRCs in the region between ambulacra, a mismatch between eONR cell position and preferred direction slowly accrues until it is zeroed at the onset position of the next ambulacrum (see Supplementary Information, Fig. S1).

Given the firing rate r_i^{ONR} and the preferred direction of each eONR cell i , the population vector was built as the vector sum of the vectors \mathbf{z}_i^{ONR} , each weighted by the firing rate of the cell, r_i^{ONR} :

$$\mathbf{v}_{pop} = \sum_{i=1}^{N_{ONR}} r_i^{ONR} (\cos(\phi_{i,pref}^{ONR}), \sin(\phi_{i,pref}^{ONR})), \quad (13)$$

where we have used notation (x, y) for a vector with components x and y , respectively. Note that, unlike the single cells preferred directions, the population vector depends on the stimulus $X(\phi)$ (via the firing rates r_i^{ONR}) and on the orientation of the stimulus with respect to the animal (see Fig. 4C-D).

Due to the recurrent connections in RNs and ONR, the neural activities need time to converge to the stationary values used in Eq. 13. Thus, we ran a simulation of the neural dynamics until the activity in the RN and ONR neurons reached the steady state. At this stage, we computed the population vector according to Eq. 13. We considered the steady state reached when the firing rates in two consecutive steps were smaller than 10^{-5} . Note that convergence to steady state occurred rapidly: Typically, in less than 200 iterations and never more than 600. Assuming a time step of 0.1 ms for each iteration (a customary choice in the literature on neural systems), this means that convergence occurred typically in about 20ms and never more than 60ms, well below the typical time scales of locomotion in *D. africanum*.

The population vectors in the presence of 3 stimuli are shown in Fig. 4C for all possible orientations of the animal with respect to the center of the stimulus. Visible stimuli are those for which there is a subset of orientations for which the population vector exceeds θ_p (red circle in figure). For animations of this figure, see the Supplementary Information, Sec. A.2.

2.4.2 Inference of visual detection based on the population vector

According to our model, the ability of the animal to detect the visual stimulus (while at the center of the arena) depends on the population vector generated by the eONR neurons. To read out the population vector we used the following model: the animal could only see the stimulus if the population vector was at least the threshold θ . This determines whether the animal will move randomly or towards the target region of the stimulus, respectively. As a specific implementation, the final position on the wall of the arena was sampled from a circularly uniform distribution if the population vector was below threshold, and from a Gaussian distribution narrowly centered around the population vector if $|\mathbf{v}_{pop}| > \theta_p$ (with standard deviation $1/(|\mathbf{v}_{pop}| - \theta_p) \leq 1$; standard deviations 5 or 10 times larger gave the same results). In panel B of Fig. 6 we show an example of the distribution of final positions (starting from random initial orientations) obtained with this method. The distribution of final positions in this case reflects the distribution of population vectors shown in Fig. 4C (or a circularly uniform distribution if the populations vectors are all smaller than the threshold).

2.4.3 Model of movement

So far, we have linked visual detection to the population vector when the animal is located at the center of the arena. As the animal moves towards the target, however, the stimulus may appear differently (e.g., larger) to the animal, and this could cause the population vector to change as the animal moves. In this section we present a model of movement in which the animal takes several steps until it reaches the wall of the arena, where the direction at each step depends on the current population vector.

In brief, the model system will move in the direction of the population vector if the latter is sufficiently larger than the threshold $\theta_p = 5$, otherwise it will move randomly but with a bias along the direction of the previous step. In detail, the movement is a probabilistic variable that may follow one of two Gaussian distributions, $p_1(\mu_1, \sigma_1)$ or $p_2(\mu_2, \sigma_2)$, depending on the length of the population vector, $v_{pop} = |\mathbf{v}_{pop}|$. Specifically, the probability of following p_1 is a logistic function of v_{pop} :

$$q(v_{pop}) = \frac{1}{1 + e^{-10(v_{pop}-\theta_p)}}, \quad (14)$$

while $1 - q(v_{pop})$ is the probability of following p_2 . Now, p_1 is a Gaussian distribution peaked around the population length, i.e., μ_1 is the direction of \mathbf{v}_{pop} and $\sigma_1 = \max\{\frac{10^\circ}{v_{pop}-\theta_p}, \epsilon\}$, where $\epsilon = (10^{-5})^\circ$ is a small number to keep the standard deviation σ_1 positive. Also, values of σ_1 larger than 360° were set to 360° (uniform distribution on the circle). The Gaussian distribution p_2 is instead peaked around the previous direction of motion, ϕ_{pre} , with fixed standard deviation $\sigma_2 = 10^\circ$ (on the first step, ϕ_{pre} was randomly sampled from a uniform distribution on the circle). The bias towards the previous direction helps to reduce the frequency of sharp directional changes, which are rarely observed experimentally.

We can conveniently describe this model in a more concise way: at each time step the movement will follow a mixture of two Gaussian distributions,

$$P(\phi_{next}|\mathbf{v}_{pop}, \phi_{pre}) = q(v_{pop}) \times p_1(\phi_{next}|\mathbf{v}_{pop}) + (1 - q(v_{pop})) \times p_2(\phi_{next}|\phi_{pre}), \quad (15)$$

where $P(\phi_{next}|\mathbf{v}_{pop}, \phi_{pre})$ is the probability of the next step ϕ_{next} given the current value of the population vector (both direction and length) and the direction of the previous step. For large population vector lengths v_{pop} , p_1 is almost certainly chosen, and it will be narrowly peaked around the direction of \mathbf{v}_{pop} ; on the other hand, if v_{pop} is below the threshold, the most likely movement will be a random step in a range of about 10 degrees from the previous direction. The probabilistic nature of this model is especially relevant for peri-threshold stimuli, for which one expects the largest behavioral variability since $p_{1,2}$ have an equal probability of being selected.

2.4.4 Simulations of behavioral trajectories

Each behavioral trial started with the animal located at the center of the arena with a random orientation ψ with respect the center of the stimulus (Fig. 5). Given a stimulus $X_0(\phi')$ at location ϕ' on the arena wall, the input to the PRCs was $X(\phi' - \psi) = X(\phi)$ in the coordinate system of the sea urchin (Eq. 3). We scaled the radius of the arena to be 1 and discretized the movement of the animal to occur in small steps $\delta r = 0.1$ at discrete points in time. Thus, rather than moving straight to the wall, the animal only made a small step and established the direction of the next step according to the stimulus detected in the current position. The length of each step roughly mimics the number of steps required to reach the wall of the arena during the experiments. We also assumed the animal does not rotate during movement as observed in experiment, in other words, the orientation of the unit vectors $\hat{\mathbf{e}}_1, \hat{\mathbf{e}}_2$ specifying the coordinate system of the animal (Fig. 5) does not change during locomotion, which empirically seems, at least approximately,

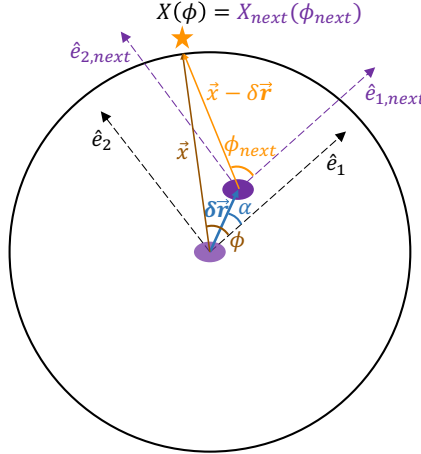


Figure 5: Stimulus coordinates during simulation of movement. The unit vectors $\hat{\mathbf{e}}_1$ and $\hat{\mathbf{e}}_2$ are the principal axes of the coordinate system of the sea urchin (purple ellipsoid). $\hat{\mathbf{e}}_i$ is the direction of the first ambulacrum in the coordinate system of the arena. The animal moves without rotating, so that the orientation of its axes remains constant (i.e., $\hat{\mathbf{e}}_{1,next} = \hat{\mathbf{e}}_1$ and $\hat{\mathbf{e}}_{2,next} = \hat{\mathbf{e}}_2$). The relative position of the yellow star with respect to the sea urchin is at ϕ when the animal is at the center of the arena, and at position ϕ_{next} after the animal has made one step $\delta\mathbf{r}$. From the new position, the stimulus appears as a new stimulus X_{next} , which is then used to compute the next movement, and so on until the animal reaches the wall of the arena and its final position is recorded.

correct. After each step, we updated the position of the animal by sampling the new position from the distribution Eq. 15, which in turn depends on its population vector and the previous position.

The procedure is illustrated in Fig. 5. Starting at the center of the arena and facing stimulus X , the animal moves to a new position $\delta\mathbf{r}$ along, say, direction α : $\delta\mathbf{r} = (\delta r \cos \alpha, \delta r \sin \alpha)$. The intensity of the stimulus at the representative location \mathbf{x} of the yellow star (in the coordinate system of the animal), is now detected at position $\mathbf{x} - \delta\mathbf{r}$, forming an angle ϕ_{next} from the first ambulacrum. Given $\mathbf{x} = (\cos \phi, \sin \phi)$ and $\mathbf{x} - \delta\mathbf{r} = (\cos \phi - \delta r \cos \alpha, \sin \phi - \delta r \sin \alpha) \doteq (v_x, v_y)$, the new angle ϕ_{next} is given by

$$\phi_{next} = \tan^{-1} \left(\frac{v_y}{v_x} \right) \quad (+180^\circ \text{ if } v_x < 0), \quad (16)$$

and the yellow star is detected as having intensity $X_{next}(\phi_{next})$ from this new position. Note that in this new position, a different point on the wall faces the animal in the direction parallel to the \mathbf{x} vector, that is, the stimulus appears as a new stimulus X_{next} , which is then used to compute the next movement (see the Supplementary Information, Sec. A.3, for animations). The trial ended when the animal reached the wall of the arena. Since *D. africanum* has long spines, we modeled its radius as being 1/4 of the distance between the wall and the center of the arena. Therefore, when the center of the sea urchin reached a distance 3/4 from the center of the arena, the animal had reached the wall and the simulation stopped. The current position at this point was projected orthogonally on the arena wall and logged as the final position.

To obtain a dataset including M animals, this procedure was repeated M times for each stimulus, each time with an animal starting from the center of the arena and with a uniformly random orientation of the first ambulacrum. As an aggregate measure of the final positions across a population of model sea

urchins, we took the circular mean vector (Blevins and Johnsen, 2004; Kirwan et al., 2018)

$$\mathbf{r}_f = \frac{1}{N} \sum_{k=1}^N (\cos \alpha_k, \sin \alpha_k), \quad (17)$$

where α_k is the final position of model sea urchin # k (relative to the line joining the center of the area to the center of the stimulus), N is the total number of sea urchins, and we have used again notation (x, y) for a vector with components x and y , respectively. The circular mean vector \mathbf{r}_f is shown as the red vector in Fig. 6B. For a narrow concentration of final positions around a given direction, \mathbf{r}_f will point towards that direction and will have a large length (i.e., close to 1). Conversely, for a uniform distribution of final positions, \mathbf{r}_f will have a length close to zero.

3 Results

3.1 Model prediction of object taxis in *Diadema africanum*

Our model of decentralized vision was built to explain the behavior of *D. africanum* in taxis experiments (Kirwan et al., 2018). In this work, individuals of this species were located at the center of an arena in the presence of three stimuli, a 40° bar stimulus and two DoG stimuli of 29° and 69°, respectively. A schematic illustration of the arena is shown in Fig. 1A; the stimuli are shown in Fig. 1B and their mathematical characterization is given in Table 1 (see the Methods for full details).

The behavioral results found by (Kirwan et al., 2018) are shown in Fig. 6A. In summary, the sea urchins moved randomly in the presence of a homogeneous stimulus of constant intensity $X_0(\phi) = 0.72$ that was used as control (Fig. 6A, top left panel). Similarly results were obtained in the presence of a 29° DoG stimulus (Fig. 6A, top right). Some coherent movement towards a 40° bar stimulus was detected, however its statistical significance was unclear (Fig. 6A, bottom left); and finally, there was clear (significant) movement towards to center of a 69° DoG stimulus (Fig. 6A, bottom right).

Significant aggregate behavior towards the 69° DoG stimulus was not merely due to a larger number of subjects used in this task ($n = 96$) compared to the same task with the other two stimuli (see (Kirwan et al., 2018) for details). The red vector at the center of the arena is the circular mean vector (Eq. 17). The direction of this vector indicates the circular mean orientation of all bearings, while the length of the arrow indicates the ‘mean resultant length’, a measure of the concentration of the points along the direction of the arrow (the longer the arrow, the more coherent directional motion in the direction of the arrow compared to the uniform distribution; a short arrow indicates random direction of movement (Kirwan et al., 2018)).

The experimental results are accurately predicted by the model, as shown in Fig. 6B. Model sea urchins with random orientations were located at the center of the arena, and the final position in each case was inferred from the initial value of the population vector. The population vector is a readout of the activity of excitatory cells in the ONR (eONR; see Methods and Fig. 4C), and reflects the activity of the PRCs and the RNs projecting to the ONR from the five ambulacra as well as the organization of the model nervous system (Fig. 3B and Methods, Sec. 2.4.1). Based on the population vector, we codified a potential mechanism by which coherent motion may be generated given information from the PRCs. The mechanism is as follows: When the length of the population vector is below a threshold $\theta_p = 5$, the sea urchin will move in random directions. The visual stimulus is detected only when the population vector length is larger than θ_p . Movement will then occur (on average) along the direction of the population vector. This is the result of integrating light information coming from all PRCs distributed

on the animal's body, mediated by neural activity in each RN, and finally integrated in the ONR (see Methods for details). Visual detection will depend on the relative position of animal and stimulus on the arena wall.

As shown in Fig. 4C, the population vector is always below threshold for the 29° DoG and the 40° bar, predicting random motion as confirmed in Fig. 6B. For the 69° DoG stimulus, the population vector length exceeds the threshold when the region of the animal's body between two ambulacra is facing the 'target region' of the stimulus (roughly, the dark region flanked by the white maxima; see Fig. 4D, rightmost plot). This means that, averaging across all initial orientations, there will be detectable motion towards the target, as confirmed in Fig. 6B (bottom right). The simultaneous activation of the activities in PRCs, RNs and ONR neurons, together with the resulting population vector readout in the ONR, can be appreciated in the animations presented in the Supplementary Information (Sec. A.2).

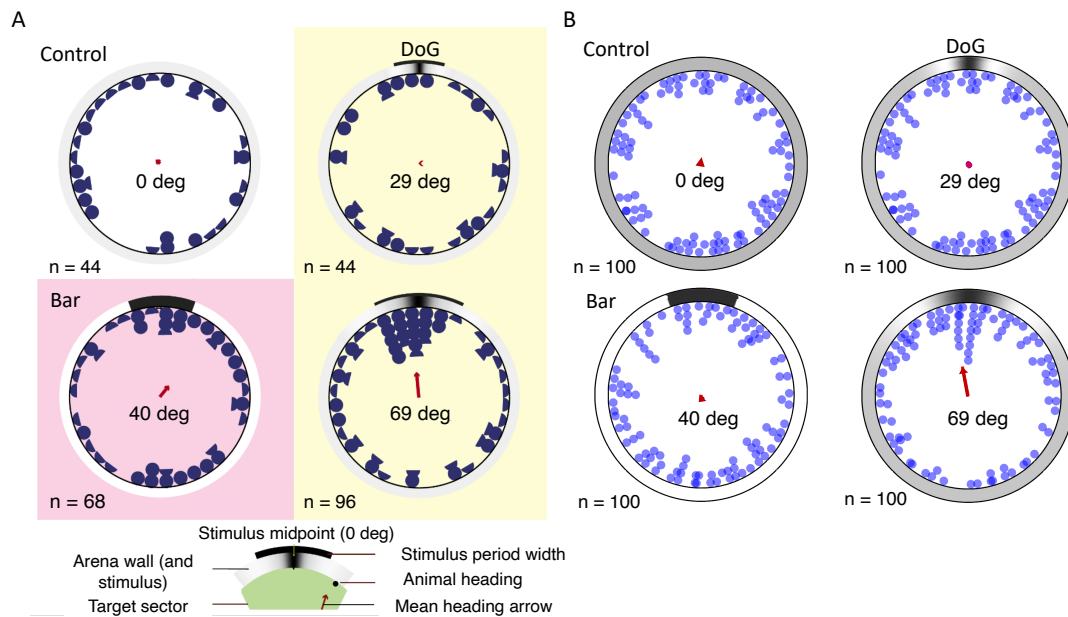


Figure 6: Behavior of model and *Diadema africanum* in the presence of 4 different stimuli.

A. Experimental results from (Kirwan et al., 2018). Each blue semicircle represents the final position of the animal at the end of one trial, while a full blue circle represents the final position of two animals. Although all animals reached the wall of the arena, final identical positions were stacked to show all the data. The stimuli used were a homogeneous stimulus with $X_0(\phi) = 0.72$ for all ϕ (control; top left panel); a 29° DoG stimulus (top right); a 40° bar (bottom left); and a 69° DoG (bottom right; see Fig. 1 and Table 1 for details about the stimuli). In each panel, the stimulus is shown on the outer wall of the arena (large circle). The red arrow at the center of the arena is a measure of aggregate directional movement across each cohort of subjects (see below). **B.** Model results in simulations of the same tasks shown in panel A. Each blue circle corresponds to one predicted final position across a cohort of 100 animals with random initial orientations with respect to the center of the stimulus. Here, the final position was inferred from the population vector (see Sec. 2.4.1) induced by the stimulus when the animal was at the center of the arena. In both panels, the red arrow at the center of each plot is circular mean vector of the final positions, i.e., \mathbf{r}_f of Eq. 17. Main parameters: $\Delta\rho = 30^\circ$, $\delta = 15^\circ$, $\theta_p = 5$ (see Table 2 for all other parameter values). Panel A adapted from (Kirwan et al., 2018).

3.2 Prediction of behavioral trajectories

In the previous section we have inferred the final position of the animal based on its ability to detect the stimulus when located at the center of the arena. This method assumes that the initial population vector not only establishes whether the stimulus has been detected, but it is also a proxy of the final position of each bearing. In the experimental results shown in Fig. 6A, however, the final position was determined based on the projection, on the arena wall, of the line connecting the center of the arena with the location of the animal at one quarter of the radius of the arena (Kirwan et al., 2018).

As the detection of the stimulus depends on the relative distance and orientation of the animal from the stimulus center during movement, the animal can adjust its movement direction according to the new visual information as it moves along in the arena. To take this into account, we generalized our model to include a basic mechanism of movement. Specifically, we discretized the animal's movement into steps and predicted the movement direction of the next step based on the stimulus as detected by the animal at the current position as well as the direction of previous movement (see Sections 2.4.3 and 2.4.4 for details). Fig. 7 shows the simulated trajectories for the same four stimuli shown in Fig. 6B (full animations for representative trials are reported in the Supplementary Information, Sec. A.3). Each colored curve is the trajectory in one out of 100 trials and the final position is marked by a dot of the same color. To take into account the fact that *D. africanum* has long spines, we assumed that the animal's body had a radius of 1/4 of the distance between the wall and the center of the arena, and each simulated trial stopped when center of the sea urchin (marked by the colored dot) reached such distance from the wall (see Sec. 2.4.4).

The distributions of predicted final positions agree well with those in Fig. 6B, suggesting that the initial movement produced at the center of the arena is, on average, a valid proxy for the final position reached using this simple model of behavior. Under control, the trajectories started off a random direction and did not change direction except for small random changes around the previous direction (Sec. 2.4.3). For the 29° DoG, initial movement was random but it would occasionally turn towards the stimulus. This happened when the location of the animal was such that light coming from the white maxima of the DoG struck one ambulacrum, causing a strong activation of PRCs at that location. For the 40° bar, the animal moved randomly at first but changed movement direction later in several trials. These changes occurred close to the stimulus target (the black region), which became wider in reference to the size of the animal as the latter approached the arena. On the opposite side, the bright region of the stimulus became narrower so that fewer ambulacra were activated. This resulted in a longer population vector and a change of movement direction towards the opposite side (this is due to a reduced cancellation of visual information that would occur when uniform light comes from most directions). Compared to the 'static' model of Fig. 6B, we noticed a smaller fraction of animals reaching the wall near the target region, although this caused no appreciable difference in the circular mean vector. Finally, for the 69° DoG, the animal would turn towards the target region when the latter faced directly one ambulacrum. In this case, due to the 69° arc subtended by the stimulus, each of the two white maxima of the stimulus would face one ambulacrum, producing a large population vector in the direction of the target region (see the rightmost plot in Fig. 4D). As a result, there was a significant concentration of final positions near the target stimulus, as also observed in Fig. 6B (bottom right).

3.3 Effect of location and acceptance angle of PRCs on spatial vision

The results shown so far were obtained assuming a longitudinal distribution of PRCs with half-width $\delta = 15^\circ$ and acceptance angle (the half-width of the angular sensitivity function) of $\Delta\rho = 30^\circ$. Together, this results in an effective acceptance angle of 60° (Fig. 4A). Varying either δ or $\Delta\rho$ can affect detection

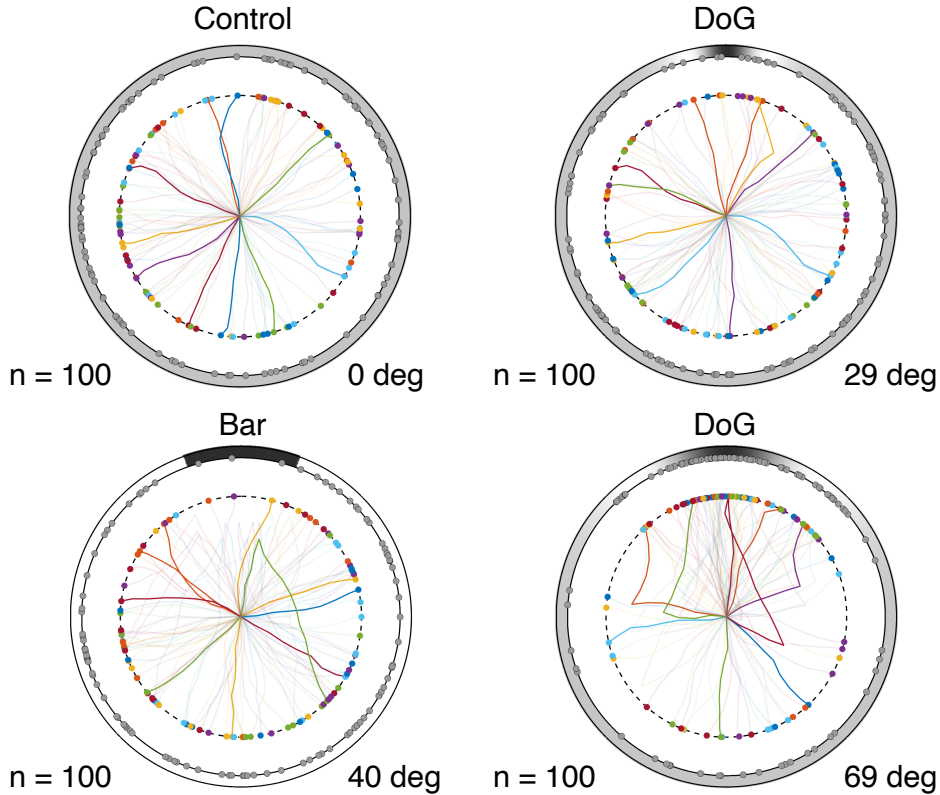


Figure 7: Simulated trajectories of 100 bearings under control, 40°bar, 29° DoG and 69° DoG stimuli. The outer circle represents the wall of the arena with the stimulus on it. Animals were placed at random orientations at the center of the arena and moved according to the behavioral model described in Sec. 2.4.3 (see also Sec. 2.4.4 for details on the simulations). The colored lines represent the trajectories covered by the center of each animal starting from the center of the arena and ending at the color-matched dot. The grey dots on the arena's wall are the radial projections of the colored dots and represent the points where the animal's body hits the wall. The same parameters as in Fig. 6B were used (see Table 2).

acuity (the minimum angular width of a visual stimulus which can be detected). For example, the reason why the model fails to detect the 29° DoG stimulus is the small arc length separation of the white maxima of the stimulus (the latter can only activate PRCs located on one ambulacrum; see Fig. 4C-D). A larger distribution width or a larger acceptance angle, however, could allow the activation of PRCs on two ambulacra, as it occurs in the 69° DoG. Is our model robust to variability of δ and $\Delta\rho$? In other words, what range of values can be allowed for these parameters so that the model still captures the results of Fig. 6A?

To answer this question, we computed the maximal length v_{max} of the population vector, Eq. 13, across all possible orientations. This was done for all values of $\Delta\rho$ between 15° and 90° and δ between 5° and 20°, and for a wide range of stimuli (Fig. 8). If, for a given pair $(\Delta\rho, \delta)$, one has $v_{max} > \theta_p$, then the stimulus can be detected (a more realistic criterion is to require a finite range of initial orientations for which the population vector length exceeds θ_p). Note that the range of $\Delta\rho$ values used here contains

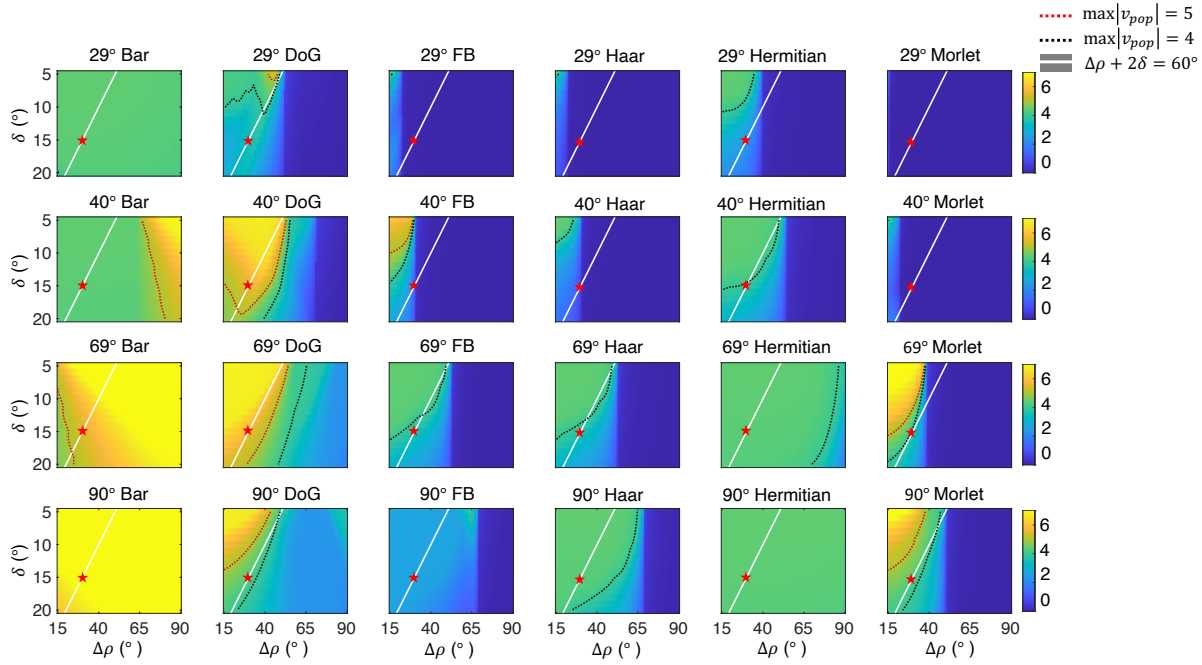


Figure 8: Effect of acceptance angle and location of PRCs on the model’s spatial vision. Each panel shows a heat map of v_{max} , the maximal length of the population vector across initial orientations of the animal, for a given stimulus and a given pair of values for $\Delta\rho$ and δ . Each column shows the same stimulus for different arc widths of the target region (i.e., for different ϕ_{stim} , see Table 1), while each row shows the same ϕ_{stim} across different stimuli. If $v_{max} < \theta_p$, the animal cannot detect the stimulus from any orientation. The red dotted line is the contour line where $v_{max} = \theta_p$, while the black dotted line is the contour line where $v_{max} = 4$. The white line is the collection of points with $\Delta\rho + 2\delta = 60^\circ$. In each plot, $\Delta\rho$ ranged between 15° and 90° and δ ranged between 5° and 20° . Red stars mark the point $(\Delta\rho, \delta) = (30^\circ, 15^\circ)$, the parameter values used in the main simulations. *DoG*: Difference of Gaussians; *FB*: Flanked bar.

our previously estimated range based on contrast thresholds between 5 and 20% (Kirwan et al., 2018).

Fig. 8 shows the value of v_{max} for different values of $\Delta\rho$ and δ . In each plot, the red dotted line is the contour line where v_{max} reaches the boundary defined by the threshold (θ_p). The animal is able to detect the stimulus for parameter values $(\Delta\rho, \delta)$ inside the yellow region delimited by the red dotted line. The red stars mark the pair of parameter values $(\Delta\rho, \delta) = (30^\circ, 15^\circ)$ used in Fig. 6B. The point defined by this pair is located outside the yellow region for the 40° bar and 29° DoG, whereas it is inside the yellow region for the 69° DoG stimulus. This implies an animal with $(\Delta\rho, \delta) = (30^\circ, 15^\circ)$ can detect the 69° DoG, but not the 40° bar and 29° DoG, as already established. Fig. 8 also shows that our results are robust to some degree of parameter variation, in the sense that they hold in a finite region of parameters space around the point $(\Delta\rho, \delta) = (30^\circ, 15^\circ)$.

Our model makes other interesting predictions. For example, it predicts that the impact of $\Delta\rho$ on spatial vision depends on the stimulus. For some stimuli (e.g., the bar) detection improves for larger $\Delta\rho$, while for other stimuli (e.g., the DoG and the Morlet wavelet) detection improves for smaller $\Delta\rho$. Furthermore, the model can be used as a guide for choosing probing stimuli in future behavioral experiments. For example, the model predicts that a 69° bar stimulus should be easily visible, whereas a 69°

Flanked bar, Haar wavelet, or 1st Hermitian wavelet stimulus should be hard to detect from any initial orientation. We emphasize that these predictions – which can be tested in experiment – depend on the neural model built in this study, and not just the properties of the PRCs.

Finally, note that in Fig. 8 we have assumed an equal acceptance angle $\Delta\rho$ for all PRCs, which is unreasonable. To address this issue, we performed the same analysis using a random distribution of $\Delta\rho$ values across PRCs in each ambulacrum. As shown in the Supplementary Information (Sec. A.4), a random distribution of $\Delta\rho$ values does not alter the general picture shown in Fig. 8 (compare Fig. 8 with Fig. S2).

4 Discussion

4.1 A model of decentralized vision in sea urchins

In this work we propose a model of decentralized vision in sea urchins based on general anatomical features of their nervous system and assuming that light information is captured by photoreceptor cells (PRCs) distributed over the animals' dermis around the ambulacra. PRCs have been found on the tube feet of sea urchins (Agca et al., 2011; Lesser et al., 2011; Ulrich-Lüter et al., 2011), which emerge from the test of the animal along the five ambulacra. The model considers the nervous system of the animal in some degree of detail, and provides a mechanistic model involving all stages of the system, from PRCs to neural activity in the ONR. PRCs on the tube feet of the animal, once activated by light, inhibit RN neurons in the same ambulacrum. In turn, RN neurons inhibit excitatory neurons in the ONR (eONR). Lateral recurrent connections in the ONR allow to integrate the information coming from all ambulacra. The activity of ONR is read out as a ‘population vector’. The population vector collates the preferred directions and the activity of all eONR neurons in the presence of a specific visual stimulus. When the length of the population vector is large enough to exceed a threshold, enough evidence has been accrued about the location of a visual stimulus, and movement towards said location occurs with probability proportional to the length of the population vector. We discuss below the feasibility of all these putative mechanisms in light of the available experimental evidence.

The model explains in quantitative detail the behavior of *D. africanum* found in the taxis discrimination task of (Kirwan et al., 2018), where taxis was found clearly only in 69° isoluminant DoG stimuli, but neither in narrower DoG nor in a 40° bar stimulus. The latter finding was somewhat surprising given that there is a much greater local contrast in the case of the bar stimulus and greater amplitude at low spatial frequencies (see Fig. 4 of (Kirwan et al., 2018)). Our model provides a mechanistic explanation of these results based on generic anatomical features of the nervous system of sea urchins combined with a specific mechanism of visual integration and readout at the level of ONR neurons.

4.2 Lessons from lesion studies

Our model uses a mechanism of double inhibition: from PRCs to RN neurons, and from RNs to the input stage of the ONR. The latter is assumed to comprise inhibitory neurons, which in turn target excitatory ONR neurons responsible for vision and locomotion. In this model, the more the RNs are inhibited by light, the larger the response of target ONR neurons leading to stimulus detection. The same results could be obtained with double excitation: PRCs excite RN neurons, which in turn will excite ONR neurons. The reason for favoring the double inhibition model is related to the findings of Yoshida in the sea urchin *Temnopleurus torematicus* (Yoshida, 1966) (see their discussion at pp. 455-456), which

we briefly review below. The putative inhibition of RN neurons in response to light is also reminiscent of the ‘off’ response of isolated RNs observed in the sea urchin *D. setosum* (Takahashi, 1964), and in general, our model’s assumption that excitatory RN neurons are inhibited by a stimulus resonates with the notion, based on early electrophysiological experiments, that RNs are a locus for interaction between excitation and inhibition (Millott and Okumura, 1968).

In the experiments described in (Yoshida, 1966), four ambulacra were surgically removed and the animal placed in dim light (under photographic safelight). Under these conditions, the majority of animals moved in the direction of the surgically operated area. Assuming positive phototaxis as the most likely behavior in this experiment (wherein the animal moves towards the light source), this finding could be explained if RN neurons inhibited ONR neurons: the removal of RNs would remove an inhibitory factor, increasing the activity of ONR neurons close to the operated area, and producing locomotion in that direction. In a related experiment, a light source was positioned outside of the animal facing the intact RN, and movement towards the light source usually ensued. This is consistent with inhibition of the intact RN by the photo-stimulated PRCs. This inhibition must cause a stronger excitation of the ONR neurons near the intact site, compared to the excitation caused by the absence of RNs on the (operated) opposite site.

When the light source was located *internally* and near the surgically operated site, locomotion in the direction of the intact RN was reduced but was still more likely than locomotion in the opposite direction. This may be because RNs can sense light directly, although to a smaller degree than when stimulated directly by PRCs. In our double inhibition model, this smaller light detection causes a smaller inhibition of the intact RN and therefore a smaller disinhibition of ONR neurons near the intact side, explaining (i) the preferential locomotion towards the intact side, but also (ii) the presence of locomotion towards the opposite side (caused by the absence of RNs on that side). Analogous experiments with two intact RNs (instead of one) led to analogous conclusions (Yoshida, 1966).

By adopting a double inhibition model, we can quantitatively explain the locomotion experiments in *D. africanum* while also capturing, at least qualitatively, the observations in surgically operated sea urchins. In this sense, the model makes strong predictions on the patterns of connections between PRCs, RN neurons and ONR neurons.

In the same article, Yoshida reported another finding that supports the integrative role ascribed by our model to the ONR. Specifically, transecting one RN near the ONR resulted in lack of motion in the direction of the transected nerve, when the animal was placed between two light sources facing each other. Thus, the ONR may play a key role in integrating visual stimuli from RNs. In our model, we have specified a possible mechanism of integration that could explain the results of Kirwan et al. (2018).

4.3 Input from mammalian physiology

The architecture of our model combines invertebrate structures with elements inspired by mammalian physiology. Examples of the former are the ganglia-like clusters of RNs connected to clusters of PRCs, and nearby clusters of RN nerves connected ‘laterally’ (see Fig. 3B) (Hyman, 1955; Matheson, 2002). This local arrangement is compatible with the fact that axons of echinoderm neurons are normally small and unmyelinated, and are bundled in packages with a parallel arrangement (Ortega and Olivares-Bañuelos, 2020). Examples from mammalian physiology include sigmoidal ‘tuning curves’ to characterize the response of RN and ONR neurons (Eq. 9). Tuning curves with similar properties are found in mammalian cortical systems of cats and primates, including primary and secondary visual neurons (Albright, 1984; Maunsell and Van Essen, 1983), middle temporal neurons (Albright, 1984; Britten et al., 1993), parietal neurons (Fanini and Assad, 2009), motor cortical neurons (Kalaska et al., 1983; Georgopoulos and Ste-

fanis, 2007; Georgopoulos et al., 1982), and so on. Similarly, reading out the activity of ONR neurons via population vectors was borrowed from landmark studies in motor and premotor cortex of primates (Kalaska et al., 1983; Georgopoulos and Stefanis, 2007; Georgopoulos et al., 1982). To date, we have no evidence that echinoderm neurons have analogous properties. Similarly, the existence of lateral connections within RN or ONR neurons is yet to be proved. However, pulling together the activity of many ONR neurons to infer the strength of visual detection and the stimulus direction is a natural and intuitive idea. These notions are both natural and parsimonious in the context of a population coding framework, wherein the coordinated activity of many neurons determines the behavior of the entire organism (Pouget et al., 2000). In the absence of more detailed experimental evidence, we have chosen to follow these principles.

We prefer also not to commit to more complex interpretations of the population vector. For example, while the length of the population vector clearly reflects the animal's ability to detect the stimulus, it may also incorporate the animal's *motivation* to move towards (or away from) it once detected. Therefore, resolving power could be greater than the level exhibited. Also, while our model sea urchin moves towards the same direction as the population vector, the opposite convention on the meaning of the population vector would induce the opposite behavior. Thus, while the readout of the ONR neurons' activity could represent additional variables related to motivation or other determinants of the behavior, we feel that it is premature to commit to any of them due to the lack of proper experimental data that could dissect the relative contributions of such variables. At this stage, the population vector is best understood as the link between the neural activity produced by the nervous system of our model, and the observed orienting behavior of *D. africanum*.

4.4 Questions for future experiments

It is an important question to determine experimentally to what degree our anatomical assumptions hold. Much information is lacking on the nervous system of Echinodermata, partly due to technical difficulties (Ortega and Olivares-Bañuelos, 2020). In the absence of more detailed information, our assumptions allow an explanation of vision in *D. africanum* – at least pertaining to the experiments performed in (Kirwan et al., 2018) – and allow to make clear predictions for future experiments. In turn, the model presented here can be modified and improved on the basis of new experimental evidence, which may alter its functionality to different degrees. To this aim, future anatomical, morphological and behavioral experiments should help clarify issues such as the impact of PRCs input onto clusters of RN neurons; the nature of neural connectivity, including the details of the excitatory vs. inhibitory action exerted by clusters of RN and ORN neurons on their target structures; the electrophysiological response of the same neurons to luminous stimuli (their 'tuning' properties); and the detailed nature of ONR integration of RN input. Furthermore, the aggregate response of ONR neurons to luminous stimuli could reveal the details of the mechanism used by these organisms to produce visually-driven behavior (here modeled via the population vector). Finally, comparison of our predictions with behavioral experiments conducted with various stimuli as shown in Fig. 8, could give indirect information on the distribution of PRCs, their (effective) angular sensitivity, and more in general on the architecture of the model upon which the predictions of that figure are based.

5 Acknowledgments

This work was supported by a Research Grant from the Human Frontiers Science Program (Ref.-No: RGP0002/2019). We thank Drs. Esther Ullrich-Lüter and Carsten Lüter for very useful discussions, and Drs. Esther Ullrich-Lüter and Michael Bok for a careful reading of the manuscript.

A Supplementary information

A.1 Analytical formula for the preferred directions of eONR cells

Here we show how to compute analytically the preferred directions of eONR cells required in the definition of the population vector, Eq. 13 of the main text. To do so, we associate unique vectors to each PRC, RN neuron and eONR neuron, and in each case define their preferred direction as the orientation of the associated vector. We then show that this definition matches the definition of preferred directions of eONR cells given in the main text.

First, consider the unit vector $\hat{\mathbf{z}}_i^{k,PRC}$ associated to PRC i on ambulacrum k having direction of maximum sensitivity $\phi_{i,dms}^{k,PRC}$,

$$\hat{\mathbf{z}}_i^{k,PRC} = (\cos \phi_{i,dms}^{k,PRC}, \sin \phi_{i,dms}^{k,PRC}), \quad (\text{A.1})$$

where $\phi_{i,dms}^{k,PRC}$ is defined in Sec. 2.3.2 of the main text. $\hat{\mathbf{z}}_i^{k,PRC}$ is a vector with unit length and orientation $\phi_{i,dms}^{k,PRC}$.

We next associate a vector to each RN neuron by taking the linear combination of all PRC vectors connected to it, where the connection weights are used as coefficients of the linear combination:

$$\mathbf{z}_i^{k,RN} = \sum_j W_{RP}^k(i,j) \hat{\mathbf{z}}_j^{k,PRC} = \overline{W}_{RN}^k \sum_{j \in conn} \hat{\mathbf{z}}_j^{k,PRC}, \quad (\text{A.2})$$

where $conn$ is the set of PRCs connected to the RN cell i on ambulacrum k , and we have also used the fact that the non-zero connections $W_{RP}(i,j)$ are all equal to the same value, here called \overline{W}_{RN}^k (see Eq. 6 of the main text). Since the lateral connections among RN neuron groups are symmetric with respect to the mean direction of maximum sensitivity of afferent PRCs, the RN neurons inherit a preferred direction (the orientation of vector $\mathbf{z}_i^{k,RN}$) which is the same as the average direction of maximum sensitivity of its afferent PRCs.

We then associate a vector to each eONR cell in a similar way:

$$\mathbf{z}_i^{ONR} = \sum_{k,j} W_{OR}(i,j) \hat{\mathbf{z}}_j^{k,RN} = \overline{W}_{OR} \sum_{k,j \in conn'} \hat{\mathbf{z}}_j^{k,RN}, \quad (\text{A.3})$$

where $\hat{\mathbf{z}} \doteq \mathbf{z}/\|\mathbf{z}\|$, the sum over k is over the five ambulacra, and $conn'$ is the set of all RNs connected to the i th ONR cell via the ‘indirect pathway’ containing intermediate iONR cells (as shown in Fig. 3B of the main text). Again, the lateral connections among groups of eONR neurons do not impact the direction of \mathbf{z}_i^{ONR} , and therefore they are not included in the definition of \mathbf{z}_i^{ONR} .

By definition, the preferred direction of eONR cells is given by the orientation of their associated vectors \mathbf{z}_i^{ONR} . Fig. S1 shows that the preferred directions computed this way agree with the preferred directions obtained in response to a 2° bar stimulus – the definition used in the main text (Sec. 2.4.1).

Also note that $\phi_{i,pref}^{ONR}$ matches the orientation of the location of eONR cell i at the onset location of each ambulacrum (0°, 72°, 144°, ...), and then a mismatch linearly accrues until the location of the next ambulacrum is reached. The mismatch is due to the lack of PRCs in the region between ambulacra, and its effect on the population vector is evident from the animations discussed in Sec. A.2.

We can now also write the population vector as a function of the PRC vectors. Recall that the population vector is defined as weighted sum of the eONR vectors (Eq. 13 of the main text), or, in the

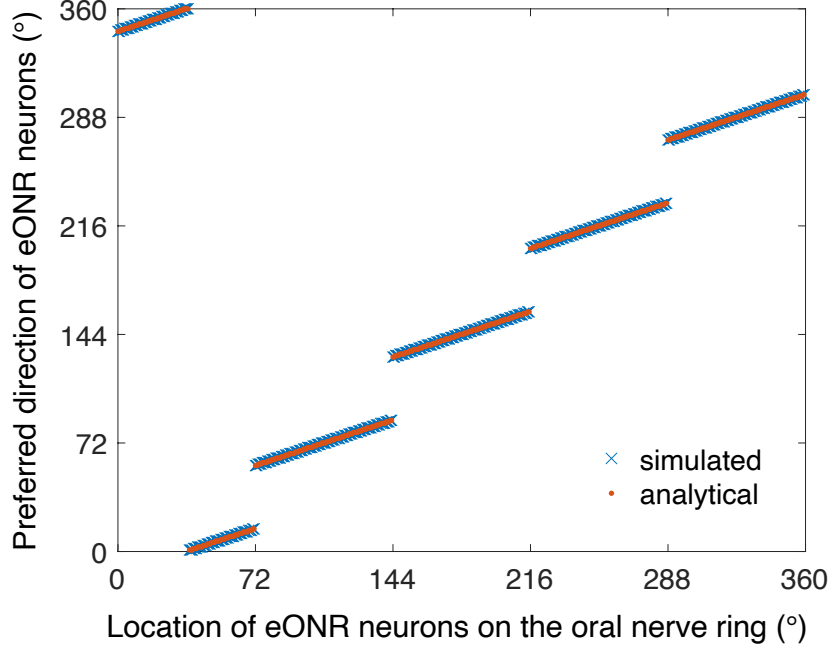


Figure S1: Comparison of preferred directions of eONR cells, defined as the orientation of vector A.3 (red circles) or as the direction of a 2° bar stimulus that causes the maximal increase in activity in the eONR cell (blue crosses). The locations at $0^\circ, 72^\circ, 144^\circ, 216^\circ$ and 288° represent the locations of the ambulacra. Starting from each ambulacrum, the preferred direction is a linear function of the location of the eONR cell with slope smaller than 1. See the text for details.

present notation,

$$\mathbf{v}_{pop} = \sum_i r_i^{ONR} \hat{\mathbf{z}}_i^{ONR}, \quad (\text{A.4})$$

where $\hat{\mathbf{z}}_i^{ONR}$ are the normalized vectors $\mathbf{z}_i^{ONR} / \|\mathbf{z}_i^{ONR}\|$. Putting together the steps leading to Eq. A.3, we obtain

$$\mathbf{v}_{pop} \propto \sum_{i=1}^{N_{ONR}} r_i^{ONR} \sum_{k,j \in \mathcal{C}(i)} \hat{\mathbf{z}}_j^{k,PRC}, \quad (\text{A.5})$$

a vector sum of PRC vectors $\hat{\mathbf{z}}_j^{k,PRC}$ weighted by coefficients proportional to the firing rates r_i^{ONR} . The sum over $k, j \in \mathcal{C}(i)$ is over all PRCs connected to eONR cell i via the ‘vertical pathway’ shown in Fig. 3B including intermediate RN and eONR cells. We note that this formula holds for our model but it does not necessarily hold for a different (especially non-symmetrical) topology of the neural connections from PRCs to ONR.

A.2 Neural activity and population vector as a function of animal orientation

Table S1 lists the URL of three animations of the activity of PRCs, RN neurons, eONR neurons and the population vector as the relative position of the animal with respect to the stimulus changes. The stimuli used were the 40° bar, a 29° DoG and a 69° DoG. To better visualize this processs, we fixed the animal's position and rotated the stimulus, which is equivalent to fixing the position of the stimulus and rotating the animal. Note how the orientation of the animal with respect to the stimulus affects stimulus detection due to the lack of PRCs between ambulacra. For narrow stimuli, this results in the existence of effective ‘blind spots’ between ambulacra.

Stimulus	URL
29° DoG	https://www.dropbox.com/s/2cmcet380m1ph23/rotation_29DoG_rho30_delta15.mp4?dl=0
40° Bar	https://www.dropbox.com/s/m25m9pocdkgfhee/rotation_40bar_rho30_delta15.mp4?dl=0
69° DoG	https://www.dropbox.com/s/ujkhzhk3b5eln4i/rotation_69DoG_rho30_delta15.mp4?dl=0

Table S1: URLs of animations showing neural activity and population vector as a function of the relative orientation of the sea urchin and the center of the stimulus.

A.3 Simulation of behavioral trajectories

Table S2 includes the URLs of three animations of the behavior of the model in response to a 40° bar, a 29° DoG and a 69° DoG. The urchin is represented by the moving circle with the 5 ambulacra drawn inside. The wall of the arena is represented by the large circle. The circle with the stimulus drawn on it and moving together with the urchin illustrates how the stimulus is ‘seen’ by the sea urchin at each new position. The red circle marks the threshold for the population vector (the latter always drawn in blue from the center of the arena). Each simulated trial ends when the edge of the urchin’s body (the smallest circle) makes contact with the arena. See Sec. 3.2 for full details.

Stimulus	URL
29° DoG	https://www.dropbox.com/s/x9jbp04g0hpkjx7/trajectory_29DoG_N10_rho30_delta15.mp4?dl=0
40° Bar	https://www.dropbox.com/s/eh1jlk3n9fpzkez/trajectory_40bar_N10_rho30_delta15.mp4?dl=0
69° DoG	https://www.dropbox.com/s/fylhsr1a7eaayf/trajectory_69DoG_N10_rho30_delta15.mp4?dl=0

Table S2: URLs of animations showing simulations of the behavior of the model in the presence of a 40° bar, a 29° DoG and a 69° DoG. All tracks comprising 100 simulations per stimulus are shown in Fig. 7 of the main text.

A.4 The effect of variability on PRCs’ acceptance angles

The results of the main text (summarized in Fig. 8) were obtained using a constant acceptance angle for PRCs. Here we repeat the analysis of Sec. 3.3 and show that our results also hold in the case of random distributions of acceptance angles across PRCs. For concreteness, we chose, in each case, Gaussian distributions with mean $\langle \Delta\rho \rangle$ and standard deviation equal to $\langle \Delta\rho \rangle / 4$ (different choices did not qualitatively alter the results). The results are shown in Fig. S2. Except for noisier contours, the regions

of parameter space defined by the $v_{max} \geq 4$ or $v_{max} \geq 5$ appear unchanged compared to those shown in Fig. 8 for constant $\Delta\rho$.

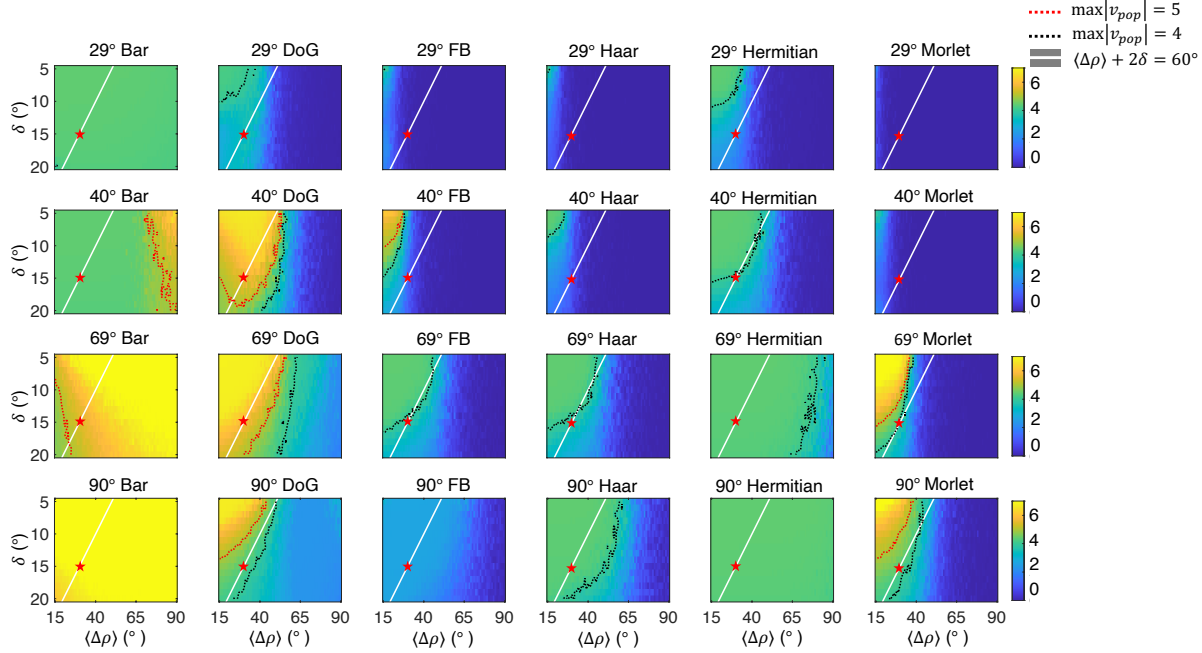


Figure S2: Effect of acceptance angle and location of PRCs on the model’s spatial vision. Same as Fig. 8 of the main text but with a random distribution of PRC acceptance angles $\Delta\rho$, chosen to be a Gaussian distribution with mean $\langle\Delta\rho\rangle$ and standard deviation $\langle\Delta\rho\rangle/4$. Each panel shows a heat map of v_{max} , the maximal length of the population vector across initial orientations of the animal, for a given stimulus and a given pair of values for $\langle\Delta\rho\rangle$ and δ . Each column shows the same stimulus for different arc widths of the target region (i.e., for different ϕ_{stim} , see Table 1), while each row shows the same ϕ_{stim} across different stimuli. If $v_{max} < \theta_p$, the animal cannot detect the stimulus from any orientation. The red dotted line is the contour line where $v_{max} = \theta_p$, while the black dotted line is the contour line where $v_{max} = 4$. The white line is the collection of points with $\langle\Delta\rho\rangle + 2\delta = 60^\circ$. Red stars mark the point $(\langle\Delta\rho\rangle, \delta) = (30^\circ, 15^\circ)$, the parameter values used in the main simulations (where, however, $\Delta\rho$ was constant across PRCs). DoG: Different of Gaussians; FB: Flanked bar.

References

- Agca C, Elhajj MC, Klein WH, Venuti JM (2011) Neurosensory and neuromuscular organization in tube feet of the sea urchin *Strongylocentrotus purpuratus*. *J Comp Neurol* 519: 3566–79.
- Al-Wahaibi MK, Claereboudt MR (2017) Extraocular vision in the sea urchin *diadema setosum*. *Marine and Freshwater Behaviour and Physiology* 50: 31–40.
- Albright TD (1984) Direction and orientation selectivity of neurons in visual area mt of the macaque. *Journal of Neurophysiology* 52: 1106–1130 PMID: 6520628.
- Barral J, Reyes AD (2016) Synaptic scaling rule preserves excitatory-inhibitory balance and salient neuronal network dynamics. *Nat Neurosci* 19: 1690–1696.
- Blevins E, Johnsen S (2004) Spatial vision in the echinoid genus *echinometra*. *J Exp Biol* 207: 4249–53.
- Britten KH, Shadlen MN, Newsome WT, Movshon JA (1993) Responses of neurons in macaque mt to stochastic motion signals. *Vis Neurosci* 10: 1157–69.
- Burke RD, Angerer LM, Elphick MR, Humphrey GW, Yaguchi S, Kiyama T, Liang S, Mu X, Agca C, Klein WH, Brandhorst BP, Rowe M, Wilson K, Churcher AM, Taylor JS, Chen N, Murray G, Wang D, Mellott D, Olinski R, Hallböök F, Thorndyke MC (2006) A genomic view of the sea urchin nervous system. *Dev Biol* 300: 434–60.
- Cobb JL (1970) The significance of the radial nerve cords in asteroids and echinoids. *Z Zellforsch Mikrosk Anat* 108: 457–74.
- Fanini A, Assad JA (2009) Direction selectivity of neurons in the macaque lateral intraparietal area. *J Neurophysiol* 101: 289–305.
- Florey E, Cahill MA (1980) Cholinergic motor control of sea urchin tube feet: evidence for chemical transmission without synapses. *J. Exp. Biol.* 88: 281–292.
- Formery L, Orange F, Formery A, Yaguchi S, Lowe CJ, Schubert M, Croce JC (2021) Neural anatomy of echinoid early juveniles and comparison of nervous system organization in echinoderms. *J Comp Neurol* 529: 1135–1156.
- Georgopoulos AP, Kalaska JF, Caminiti R, Massey JT (1982) On the relations between the direction of two-dimensional arm movements and cell discharge in primate motor cortex. *J Neurosci* 2: 1527–37.
- Georgopoulos AP, Stefanis CN (2007) Local shaping of function in the motor cortex: motor contrast, directional tuning. *Brain Res Rev* 55: 383–9.
- Holmes SJ (1912) Phototaxis in the sea urchin, *arbacia punctulata*. *J. Anim. Behav.* 2: 126–136.
- Hyman L (1955) *The Invertebrates vol. IV Echinodermata*. McGraw-Hill, New York.
- Kalaska JF, Caminiti R, Georgopoulos AP (1983) Cortical mechanisms related to the direction of two-dimensional arm movements: relations in parietal area 5 and comparison with motor cortex. *Exp Brain Res* 51: 247–60.
- Kawaguti S (1964) Electron microscopic structures of the podial wall of an echinoid with special references to the nerve plexus and the muscle. *Biol. J. Okayama Univ.* 10.

- Kirwan JD, Bok MJ, Smolka J, Foster JJ, Hernández JC, Nilsson DE (2018) The sea urchin diadema africanum uses low resolution vision to find shelter and deter enemies. *J Exp Biol* 221.
- Land MF, Nilsson DE (2012) *Animal eyes* Oxford animal biology series. Oxford University Press, Oxford, 2nd ed edition.
- Lesser M, Carleton K, Böttger S, Barry T, Walker C (2011) Sea urchin tube feet are photosensory organs that express a rhabdomeric-like opsin and pax6. *Proc R Soc B* 278: 3371–3379.
- Matheson T (2002) Invertebrate nervous systems. In *Encyclopedia of Life Sciences*. Macmillan Publishers Ltd, Nature Publishing Group.
- Maunsell JH, Van Essen DC (1983) Functional properties of neurons in middle temporal visual area of the macaque monkey. i. selectivity for stimulus direction, speed, and orientation. *J Neurophysiol* 49: 1127–47.
- Millott N, Okumura H (1968) The electrical activity of the radial nerve in diadema antillarum philippi and certain other echinoids. *J Exp Biol* 48: 279–87.
- Millott N, Takahashi K (1963) The shadow reaction of diadema antillarum philippi. iv. spine movements and their implications. *Philos. Trans. R. Soc. B Biol. Sci.* 246: 437–469.
- Ortega A, Olivares-Bañuelos TN (2020) Neurons and glia cells in marine invertebrates: An update. *Front Neurosci* 14: 121.
- Pouget A, Dayan P, Zemel R (2000) Information processing with population codes. *Nat Rev Neurosci* 1: 125–32.
- Rodríguez A, Hernández J, Clemente S, Coppard S (2013) A new species of diadema (echinodermata: Echinoidea: Diadematidae) from the eastern atlantic ocean and a neotype designation of diadema antillarum (philippi, 1845). *Zootaxa* 3636: 144–170.
- Salinas E, Abbott LF (1994) Vector reconstruction from firing rates. *J Comput Neurosci* 1: 89–107.
- Takahashi K (1964) Eletrical responses to light stimuli in the isolated radial nerve of the sea urchin, Diadema setosum (leske). *Nature* 201: 1343–4.
- Ullrich-Lüter EM, Dupont S, Arboleda E, Hausen H, Arnone MI (2011) Unique system of photoreceptors in sea urchin tube feet. *Proc Natl Acad Sci U S A* 108: 8367–72.
- Woodley JD (1982) Photosensitivity of Diadema antillarum: does it show scototaxis? In Lawrence JM, editor, *Echinoderms: Proceedings of the International Conference, Tampa Bay*, p. 61. Balkema, Rotterdam.
- Yerramilli D, Johnsen S (2010) Spatial vision in the purple sea urchin Strongylocentrotus purpuratus (Echinoidea). *J Exp Biol* 213: 249–55.
- Yoshida M (1966) Photosensitivity. In Boolootian R, editor, *Physiology of Echinodermata*, pp. 435–464. John Wiley and Sons, New York.